JOURNAL OF GEOPHYSICAL RESEARCH, VOL. 113, B12407, doi:10.1029/2008JB005655, 2008

Damage patterns, stress rotations and pore fluid pressures in strike-slip fault zones

David Healy[1]

Received 28 February 2008; revised 21 August 2008; accepted 10 September 2008; published 17 December 2008.

[1] Active faults unfavorably oriented with respect to the regional maximum compressive stress have been labeled as "weak." The seismic hazards posed by these faults make understanding this apparent weakness a priority. Stress rotations in these fault zones, together with an increase in mean stress, could enable high pore fluid pressures to weaken a fault zone. Such a model requires a foundation in the physics and mechanics of damage. This paper presents a new model for stress rotations in fault zones by combining the Effective Medium Theory with anisotropic poroelasticity. This approach enables the quantitative characterization of crack damage and the prediction of progressive changes in the elastic properties of rocks across the fault zone. The processes of fault growth and wear will lead to distinct patterns of crack damage, with different effects on the elastic properties. Elevated pore fluid pressures have long been known to change the effective normal and shear stresses of anisotropic rocks, and this work incorporates these effects into a multilayer fault zone model. It is shown that high pore fluid pressures in the anisotropic rocks of the core zone can generate large stress rotations (i.e., more fault-parallel), and increases in mean stress, sufficient to weaken the fault. Stress rotations in the damage zones of unfavorably oriented faults tend to be away from the fault (i.e., more fault-normal) for likely combinations of damage patterns and pore fluid pressure.

Citation: Healy, D. (2008), Damage patterns, stress rotations and pore fluid pressures in strike-slip fault zones, *J. Geophys. Res.*, *113*, B12407, doi:10.1029/2008JB005655.

1. Introduction

[2] Fault planes oriented at a high angle to the regional maximum compressive stress (σ_1 in this paper; $\sigma_1 > \sigma_2 > \sigma_3$) are known to be active. Such faults have been termed "weak" in comparison to laboratory predictions of frictional strength [*Byerlee*, 1978]. Subvertical strike-slip faults in the San Andreas system trend at 60–80° to the regional compression [*Zoback et al.*, 1987; *Jones*, 1988; *Hardebeck and Hauksson*, 1999; *Provost and Houston*, 2001]. Low-angle normal faults in the Altotiberina Fault system (Apennines, Italy) make an angle of 70–80° with the vertical lithostatic load [*Collettini and Barchi*, 2002], and a similar fault geometry has been found in the Woodlark Basin of the SW Pacific [*Abers*, 1991]. Given the seismic hazard posed by these structures, there is a clear need to understand the mechanics of this apparent weakness.

[3] The physical cause of fault weakness is the subject of vigorous debate. Suggested mechanisms include: inherently weak material in the fault zone [*Moore and Rymer*, 2007], dynamic weakening processes including thermal pressurization [*Wibberley and Shimamoto*, 2005] and coseismic shear heating [*Hirose and Bystricky*, 2007], and high pore fluid pressures [*Chester et al.*, 1993; *Faulkner and Rutter*, 2001]. These static and dynamic mechanisms operate over different scales of time and length. For a static weakening mechanism, the high pore fluid pressure model requires stress rotations in some part of the fault zone, otherwise σ_3 will be pushed into the tensile field. This in turn would generate hydrofractures, the loss of fluid pressure, and fault strengthening.

[4] There is evidence for inhomogeneous stress around active major faults, chiefly from focal mechanism data [*Hardebeck and Hauksson*, 1999; *Provost and Houston*, 2001] and borehole breakouts [*Chéry et al.*, 2001], although the width and precise location over which any rotations of the maximum compression occurs is debated. Models involving stress rotation within a plastic fault core [*Rice*, 1992] are problematic in that σ_1 can only rotate to 45° with the fault zone in an ideally plastic gouge material, which may not be sufficient to generate slip.

[5] *Faulkner et al.* [2006] integrated field observations and laboratory measurements with a model based on isotropic elasticity to predict stress rotations in a strike-slip fault damage zone. Their model predicts a rotation of σ_1 from 80° to the fault outside the damage zone, to about 40° at the damage zone-core interface. This rotation is a consequence of a progressive, and isotropic, change in elastic properties mapped to an exponentially increasing density of cracks toward the fault core.

[6] The model described in this paper is an extension of *Faulkner et al.* [2006], designed to explore the effects of

[1]The Institute for Geoscience Research, Department of Applied Geology, Curtin University of Technology, Perth, Western Australia, Australia.

0148-0227/08/2008JB005655$09.00

damage patterns on the elastic properties of fault zones. In particular, this work investigates different patterns of crack damage combined with the effect of pore fluid pressure to predict the state of stress across a fault zone. The new model covers the damage zone and the fault core and incorporates anisotropy and poroelasticity. The model applies to any orientation of fault plane with respect to the principal compression, but the results are presented in the reference frame of a vertical strike-slip fault. Models are used to explore the likely location of stress rotations in the fault zone, i.e., in the damage zone or in the fault core.

[7] The paper is organized as follows. Section 2 describes a simple elastostatic multilayer model for a fault zone, highlighting the effect of the layer elastic constants on the orientation of the maximum compressive stress. Section 3 critically reviews the isotropic damage zone model of *Faulkner et al.* [2006]. The application of Effective Medium Theory to fault zones is discussed in section 4. In section 5, observations of crack patterns from the damage zones of large faults are used to define idealized patterns for the subsequent models. Section 6 develops the elastic multilayer fault zone model with the addition of anisotropic poroelasticity, before section 7 describes the model predictions from various crack patterns in the damage zone. The focus shifts to the fault core zone in section 8, with model predictions for the stress state in anisotropic lithologies with crack damage. Section 9 discusses the model parameter selections, the model results with reference to the San Andreas Fault and attempts to rationalize the isotropic model of *Faulkner et al.* [2006]. The key findings are summarized in section 10.

2. Elastic Multilayer Model of a Strike-Slip Fault Zone

2.1. Model Configuration and Boundary Conditions

[8] For a vertical strike-slip fault, the fault zone is represented as a suite of fault-parallel, vertical layers (Figure 1), which are parallel to *xz* in the chosen coordinate reference frame. The fault normal direction is *y*. Each layer is elastically isotropic and assigned distinct values of Young's modulus, E, and Poisson's ratio, ν. The model is subjected to an applied stress at the outermost intact layer (Figure 1), with the maximum principal (compressive) stress σ_1 horizontal and oriented at a high angle (ϕ) to the fault plane (*xz*). Assuming mechanical equilibrium (no net rotation), plane strain in *xy* ($\varepsilon_{zz} = 0$) and with no slip between the layers (ε_{xx} = constant), the stresses and strains can be calculated for each layer in the fault zone. Changes in elastic properties between the layers produce changes in stress and strain within each layer, compared to the applied stress, and this can lead to rotations of σ_1, i.e., changes in the local value of ϕ (see *Casey* [1980] for further details).

2.2. Stress Rotations and Elastic Properties

[9] Stress rotations in the isotropic model are highly sensitive to the value of Poisson's ratio. The trace of the fault plane is parallel to *x*, and the angle between σ_1 and *x* is given by [*Jaeger et al.*, 2007]:

$$\varphi = \arctan\left[2\tau_{xy} \Big/ \sqrt{(\sigma_{xx} - \sigma_{yy}) + \left(4\tau_{xy}^2 + (\sigma_{xx} - \sigma_{yy})^2\right)}\right] \quad (1)$$

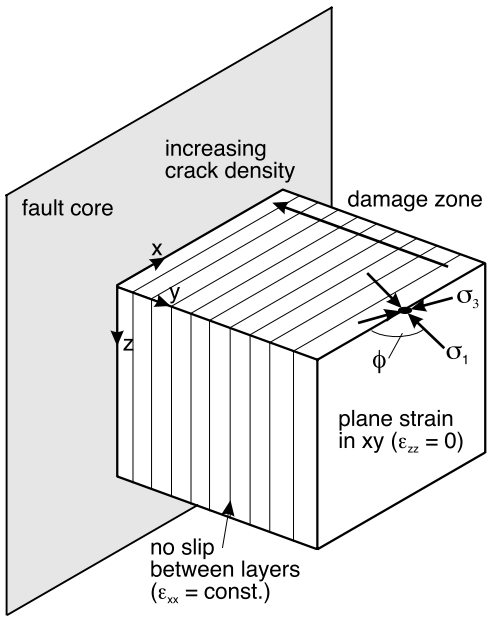

Figure 1. Configuration of the elastic multilayer fault zone model. The fault core is vertical and parallel to *xz*, and the damage zone is divided into 10 parallel vertical layers. Crack density increases toward the fault core. The boundary conditions include no slip between the layers (ε_{xx} is constant) and plane strain in *xy* (ε_{zz} is zero). A remote stress is applied at an angle $f = 80°$ and the elastic stresses and strains calculated in the remaining layers. See *Casey* [1980] for more details.

where σ_{xx}, σ_{yy}, and τ_{xy} are the Cartesian components of stress. To generate a large rotation of σ_1 toward the fault plane (i.e., decreased ϕ) requires σ_{xx} to increase with respect to σ_{yy}. The boundary condition of no net rotation restricts σ_{yy} and τ_{xy} to being constant across all the layers. Therefore, variations in ϕ in the model must originate from variations in σ_{xx}. The σ_{xx} stress component can be expressed as [*Casey*, 1980]:

$$\sigma_{xx} = c_{11}\varepsilon_{xx} + c_{12}(\sigma_{yy} - c_{21}\varepsilon_{xx})/c_{22} \quad (2)$$

where the stiffness coefficients, c_{ij}, for an isotropic material are

$$c_{11} = c_{22} = E(1-\upsilon) \Big/ [(1+\upsilon)(1-2\upsilon)] \quad (3)$$

and

$$c_{12} = c_{21} = E\upsilon \Big/ [(1+\upsilon)(1-2\upsilon)] \quad (4)$$

[10] It is clear from equations (2)–(4) that an increase in σ_{xx} within a layer can only occur through changes in E and ν. This dependence of ϕ on E and ν is shown in Figure 2. Using elastic constants for isotropic granodiorite from the Cerro Cristales pluton, northern Chile (Table 1, data from *González* [1999] and T. M. Mitchell and D. R. Faulkner, unpublished manuscript, 2007), the separate influence of E

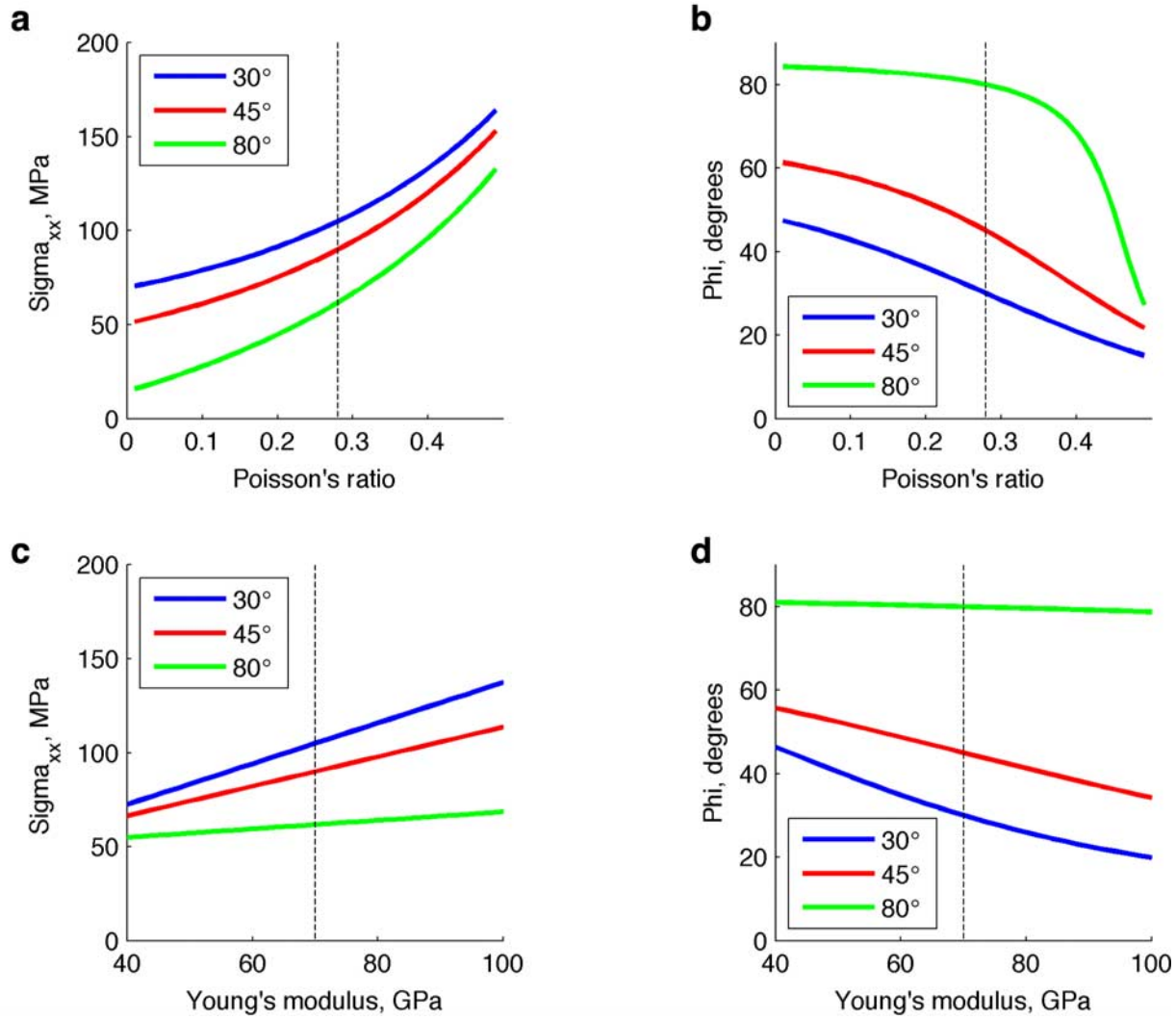

Figure 2. Graphs showing the dependence of s_{xx} and f on Poisson's ratio and Young's modulus for the isotropic multilayer model.

and ν on ϕ and σ_{xx} is shown by holding one of the elastic parameters constant and varying the other. These curves were calculated using an applied remote stress of σ_1 = 120 MPa (applied at 30°, 45° and 80° to the fault zone) and σ_3 = 60 MPa. In Figures 2a–2b, the effect of Poisson's ratio in the isotropic model is significant for the case of highly misoriented faults (ϕ = 80° outside the fault, green curves in Figures 2a–2b). For $\nu > \sim 0.4$, the rapid increase in the Cartesian σ_{xx} component drives ϕ downward to <40°. At the isotropic limit of ν = 0.5, ϕ can reach 20°. Note also that decreases in ν produce increases of ϕ, i.e., σ_1 can rotate away from the fault. The effect of changes in E is more muted (i.e., flatter curves in Figures 2c–2d), and for highly misoriented faults (green curves in Figures 2c–2d), is not significant.

3. Isotropic Fault Damage Zone Model

3.1. Predictions From the Model of *Faulkner et al.* [2006]

[11] The model for a fault damage zone used by *Faulkner et al.* [2006] is based on that of *Casey* [1980] (see above). The elastic properties were taken from uniaxially compressed samples of Westerly granite [*Heap and Faulkner*, 2008]. The samples were unconfined and the elastic properties were measured from stress-strain curves recorded over stress cycles of increasing amplitude. The initial intact values were measured as E = 69 GPa and ν = 0.27. The values for the innermost damage zone layer (closest to the fault) were taken at the end of the stress cycling and measured as E = 59 GPa and ν = 0.47. The intervening layers were assigned intermediate values scaled according to the exponential form of a crack density versus distance

Table 1. Elastic Constants of Intact Cerro Cristales Granodiorite[a]

	ci1	*ci2*	*ci3*	*ci4*	*ci5*	*ci6*
c1j	89.49	34.80	34.80	0.00	0.00	0.00
c2j	34.80	89.49	34.80	0.00	0.00	0.00
c3j	34.80	34.80	89.49	0.00	0.00	0.00
c4j	0.00	0.00	0.00	27.34	0.00	0.00
c5j	0.00	0.00	0.00	0.00	27.34	0.00
c6j	0.00	0.00	0.00	0.00	0.00	27.34

[a]Cerro Cristales granodiorite, isotropic (T. M. Mitchell and D. R. Faulkner, unpublished manuscript, 2007), Young's modulus = 70 GPa, Poisson's ratio = 0.28, Stiffness tensor c_{ij} (Voigt notation, units are GPa).

plot [*Faulkner et al.*, 2006, Figure 1]. The stresses and strains were computed for the layers in the damage zone, and the angle between the fault plane and σ_1 was shown to decrease. For a regional principal compression (σ_1) inclined at 80° to the fault plane outside the damage zone, the progressive changes in isotropic elastic properties generated a stress rotation of over 30° in the innermost damage zone layer [*Faulkner et al.*, 2006, Figure 3b].

3.2. Applicability of Elastic Properties Measured in Unconfined, Uniaxial Experiments

[12] The experimentally derived changes in elastic properties used by *Faulkner et al.* [2006] amount to a 15% reduction in E and a 75% increase in ν over the width of the damage zone. It is unclear whether experimental measurements from unconfined uniaxial tests can be applied to the damage zone of a fault exhumed from several kilometers depth, where a triaxially compressive stress regime is much more likely [e.g., *McGarr*, 1988]. Given the importance of Poisson's ratio in controlling the degree of stress rotation (Figures 2a–2b), the validity of the chosen values for the elastic properties is absolutely critical. While successful in illustrating significant stress rotations of over 30°, the simplified isotropic model presented by *Faulkner et al.* [2006] provides no explanation for the mechanism(s) responsible for generating increased Poisson's ratio within an elastically isotropic damage zone at elevated confining pressures. The work reported here is motivated by the need to find a quantitative theoretical basis for crack damage, the consequences of this damage for the elastic properties and a mechanically consistent model for inhomogeneous stress in fault zones.

4. Effective Medium Theory Applied to Fault Zone Damage

4.1. Crack Damage and Changes in Elastic Properties

[13] Macroscopic brittle faults in rock are formed by the interaction and coalescence of many microcracks [*Brace et al.*, 1966; *Lockner et al.*, 1991; *Reches and Lockner*, 1994; *Healy et al.*, 2006a, 2006b]. Experimental observations confirm that the damage produced by these microcracks changes the bulk elastic properties of the rock [*Brace et al.*, 1966]. While increases in confining pressure lead to small increases in elastic stiffness, increasing deviatoric stress toward the yield strength generates marked decreases in elastic stiffness [*Sayers and Kachanov*, 1995; *Schubnel et al.*, 2006]. Conceptually, these effects can be understood in terms of the opening and closing of microcracks along the loading path. A more rigorous and quantitative foundation is provided by the Effective Medium Theory (EMT) of *Kachanov* [1993]. Earlier theoretical approaches based on the self-consistent scheme [*O'Connell and Budiansky*, 1974] predict vanishing elastic stiffnesses at quite small crack densities (<0.2), contrary to experimental data [*Katz and Reches*, 2004; *Schubnel et al.*, 2006].

[14] The EMT approach links crack density to changes in elastic compliance. The crack density is defined as a tensor which captures the effects of an orientation distribution in the damage. The second-order crack density tensor α is defined as:

$$\alpha = (1/V)\sum\nolimits_N a^3 \mathbf{nn} \tag{5}$$

where V is the volume of interest, N is the number of cracks in this volume, and a is the radius of a circular crack, with constant unit normal **n**. This approach makes the assumption of flat, penny-shaped cracks. Note that the scalar crack density, ignoring any orientation distribution of the cracks, can be expressed as:

$$\rho = tr\,\alpha = (1/V)Na^3 \tag{6}$$

The models in this paper ignore the fourth-order crack density tensor which has no significant effect on the compliances for "dry" cracks [*Sayers and Kachanov*, 1995]. The effective compliance σ_e of a cracked rock can be written as:

$$s_e = s_i + \Delta s \tag{7}$$

where s_i is the original compliance of the intact rock and Δs describes the crack damage:

$$\Delta s_{ijkl} = \left[8\left(1-\nu^2\right)\Big/3E(2-\nu)\right]\left(\alpha_{ik}\delta_{jl} + \alpha_{il}\delta_{jk} + \alpha_{jk}\delta_{il} + \alpha_{jl}\delta_{ik}\right) \tag{8}$$

where δ is the Kronecker delta. The changes in elastic compliance are therefore a direct function of the number of cracks (N) and the orientation distribution (**n**) of these cracks. An initially isotropic rock will in general be degraded to a lower elastic symmetry due to increasing anisotropic damage, with compliance values increasing with crack density.

[15] The EMT approach depends on the Non-Interaction Approximation (NIA), which assumes the effects of each crack are isolated to allow a simple summation to compute the bulk effective change. The validity of this assumption has been demonstrated by comparing the predicted changes in elastic properties with finite element models of closely spaced and intersecting cracks [*Grechka and Kachanov*, 2006] and with experimental observations [*Katz and Reches*, 2004]. Even for high scalar crack densities up to ~0.5, the NIA holds up because for a random spatial distribution of crack centers within a rock volume, the mutually antagonistic effects of shielding and amplification in the local elastic fields of the cracks will tend to balance out.

[16] The results from rock deformation experiments support the use of EMT to describe damage evolution and the changes to elastic properties. [*Schubnel et al.*, 2003, 2006] inverted measurements of elastic wave velocities during the deformation of granite, basalt, and marble, with a good correspondence between model predictions and observations. *Katz and Reches* [2004] also validated the EMT approach by mapping microcrack damage in experimentally deformed granite samples. The detail of these laboratory studies have not, to date, been matched by field studies. *Rabbel et al.* [2004] inverted seismic velocity measurements in the KTB deep borehole to calculate elastic stiffnesses near a major fault zone. The KTB data, while sparse, show a progressive decrease in five elastic stiffness coefficients (i.e., increases in compliance) as the fault is approached at a depth of ~8 km.

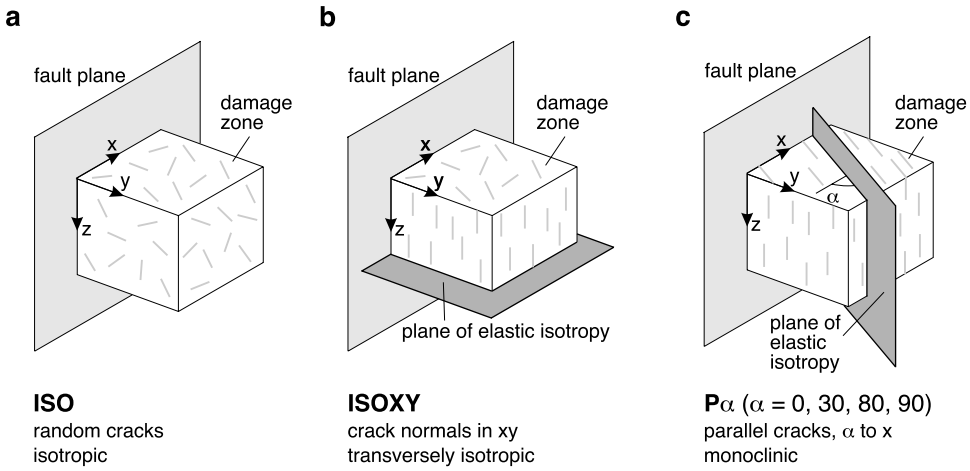

Figure 3. Schematic diagrams of crack patterns in damage zones to illustrate the effect of orientation distribution on the bulk elastic symmetry. The fault plane is vertical and parallel to *xz* in the modeled reference frame. (a) Random cracks will generate an isotropic effective medium in the damage zone. (b) Crack patterns with all poles in the *xy* plane will lead to horizontal transverse isotropy, with the plane of isotropy normal to the fault. (c) Vertical array of parallel cracks inclined at some angle α to the *x* direction. The plane of isotropy is also vertical and lies parallel to the cracks.

[17] In summary, the EMT approach of *Kachanov* [1993] provides a theoretical basis for the evolution of damage in rock and the related changes in elastic properties. Moreover, the quantitative comparison of data from samples fractured under controlled laboratory conditions [e.g., *Schubnel et al.*, 2006] confirms that the theory accurately captures the behavior of damage in a tractable form. The application of EMT to fault zones in this paper exploits the ubiquitous observation of crack density increasing toward the fault core and couples this to the observations of distinct patterns in the orientations of cracks in fault zones. The crack density tensor (α) of EMT incorporates the density of cracks and their orientation distribution. The evidence for these distinct patterns and their representation in the models are discussed next.

5. Crack Patterns in Fault Damage Zones

5.1. Observations and Conceptual Models

[18] Cracks and fractures in the volume of rock surrounding a fault increase in number toward the fault plane [*Flinn*, 1977]. Such damage zones [*Caine et al.*, 1996] form the subject of numerous field-based studies [*Chester and Logan*, 1986; *Vermilye and Scholz*, 1998; *Wilson et al.*, 2003] which consistently show an exponential increase in the number of fractures at all scales toward the fault plane. Intact rocks outside the damage zone are effectively elastically isotropic [*Anders and Wiltschko*, 1994; *Chester and Logan*, 1986], with little or no preferred orientation of cracks. The combination of increasing crack density and any preferred orientation of cracks in the damage zone will lead to effective elastic anisotropy in the damage zone and probably the core zone too.

[19] The crack damage patterns modeled in this paper are end-member idealizations derived from field observations and conceptual models of fault growth and slip. Models of fault growth are characterized by microcrack arrays oriented at a low angle, typically $\sim 30^\circ$, to the fault plane. Tensile microcracks will form normal to the local σ_3 direction, and parallel to the applied $\sigma_1 - \sigma_2$ principal plane. Faults in low-porosity crystalline rocks nucleate and grow through the en echelon interaction and coalescence of these tensile microcracks [*Reches and Lockner*, 1994; *Healy et al.*, 2006a; 2006b]. Damage accumulates at the fault tip in a process zone [*Vermilye and Scholz*, 1998; *Wilson et al.*, 2003], but repeated slip on a fault plane over many seismic cycles will drive further deformation in the wall rocks which may obscure the original fault tip patterns in mature fault zones [*Chester et al.*, 2004]. Nonplanar faults, heterogeneities in the wall rocks and asperities on the fault plane lead to stress concentrations and damage known as wear, which can generate fault-parallel and fault-normal crack arrays in the damage zone [*Wilson et al.*, 2003].

5.2. Idealized Crack Patterns Used in This Study

[20] The ISO random crack pattern has been defined for comparison with the arbitrary isotropic scaling of elastic properties in the work of *Faulkner et al.* [2006] (Figure 3a and Table 2) and generates an elastically isotropic stiffness tensor. The ISOXY pattern (Figure 3b, Table 2) consists of a vertical array of cracks and produces horizontal transverse isotropy. Such a pattern might capture the effects of many cycles of fault slip with active wear processes, in the damage zone of a vertical strike-slip fault [*Wilson et al.*, 2003]. This ISOXY pattern also matches the likely pattern of cracks in a uniaxial deformation experiment, with vertical cracks randomly oriented in the radial direction (i.e., normal to the applied load).

[21] A crack damage pattern (P30) to characterize fault growth processes consists of parallel cracks inclined at 30° to the fault plane (Figure 3c, Table 2). For a vertical strike-slip fault, this pattern imparts transversely isotropic symmetry to the elastic stiffness tensor, with a plane of isotropy oblique to the fault plane (Figure 3b). Wear processes acting along the fault can produce fault-parallel and fault-normal cracks [*Wilson et al.*, 2003], and these are captured by the P0 and P90 damage patterns (Figure 3c, Table 2). Finally, damage produced by the sustained action of a maximum

Table 2. Summary of Crack Patterns Used in Damage Zone Models

Label	Bulk symmetry	Remarks
ISO	Isotropic	Uniform distribution of cracks in *xyz*
ISOXY	Transversely isotropic (vertical symmetry axis)	Poles to cracks uniformly distributed in *xy* plane
P0	Transversely isotropic (horizontal symmetry axis)	Parallel cracks, parallel to fault plane (*xz*)
P90	Transversely isotropic (horizontal symmetry axis)	Parallel cracks, normal to fault plane (*xz*)
P30	Monoclinic	Parallel cracks, at 30° to fault plane (*xz*)
P80	Monoclinic	Parallel cracks, at 80° to fault plane (*xz*)

compressive stress at a high angle (e.g., 80°) to the fault plane will likely produce cracks in a similar orientation. The P80 pattern contains vertical parallel cracks at 80° to the fault plane (Figure 3c, Table 2), that is also transversely isotropic with the plane of isotropy at 80° to the fault (Figure 3e).

[22] Orientation distributions were defined for each of these crack patterns with a constant crack radius (0.01 m) to calculate the changes in elastic compliance with crack density using the EMT formulations for dry cracks in the work of *Sayers and Kachanov* [1995]. The calculated compliance tensors were inverted to obtain the elastic stiffnesses for the elastic multilayer model. Table 2 summarizes the attributes of the selected crack damage patterns. Note that the modeled damage patterns are based on penny-shaped cracks, i.e., infinitely thin cracks. This is in accord with the experimental data from samples deformed under nonzero confining pressure, in contrast to unconfined experiments conducted at zero (or atmospheric) confining pressure, which lead to sample volume increases due to the combined effects of cracks with finite apertures [*Brace et al.*, 1966]. The models in this paper have been designed to investigate the effects of damage patterns on stress at depths of 3–5 km, i.e., elevated confining pressure, and this justifies the use of penny-shaped cracks.

6. Anisotropic Poroelastic Multilayer Model

[23] Most (five out of six) of the crack damage patterns listed in Table 2 generate anisotropic elastic properties, due to the symmetry of the orientation distributions. For saturated rocks with pore fluid pressure (p_f) > 0, anisotropy in the form of crack damage influences the effective stress [*Carroll*, 1979; *Chen and Nur*, 1992]. In the isotropic case of effective stress, only the normal stresses acting on the solid rock skeleton are modified by the pore fluid pressure. However, structural anisotropy (e.g., nonisotropic alignments of cracks, pores) leads to changes in both the normal and the shear stresses. This has counterintuitive and important consequences for rock failure. For example, in the classical isotropic case, increases of p_f tend to move the stress state toward failure, and decreases in p_f promote stability. In the case of anisotropy, depending on the strength and orientation of the anisotropic fabric with respect to the load, the opposite effects are possible, i.e., increasing p_f can promote stability (see *Chen and Nur* [1992] for a full discussion). To model the effects of anisotropic crack patterns on the stress state in saturated fault zones, this behavior must be incorporated into the multilayer model. The original isotropic elastic multilayer formulation of *Casey* [1980] has been extended to include the effects of anisotropic poroelasticity.

[24] Incorporating anisotropic elasticity in the *Casey* [1980] model is trivial. The term for the σ_{xx} component of the Cartesian stress tensor is modified according to the symmetry of the elastic stiffness tensor, c_{ij}. For the case of isotropy (e.g., the ISO pattern), the c_{16}, c_{26} and corresponding c_{61} and c_{62} terms are 0 and do not appear in the equation for s_{xx} [cf. *Casey*, 1980, equation (5)]. For transversely isotropic elastic stiffness tensors with symmetry axes aligned with the coordinate reference axes these stiffness coefficients are also 0. This applies to the ISOXY, P0, and P90 crack patterns (Table 2). However, for monoclinic elastic symmetry (P30 and P80 patterns), the equation for σ_{xx} is now:

$$\sigma_{xx} = c_{11}\varepsilon_{xx} + c_{12}\left(\sigma_{yy} - c_{21}\varepsilon_{xx} - c_{26}\tau_{xy}\Big/c_{66}\right)\Big/c_{22} + c_{16}\tau_{xy}\Big/c_{66} \tag{9}$$

To include the effects of fluids in the anisotropic multilayer fault zone model, the effective stress in each layer is calculated according to the following equation [*Chen and Nur*, 1992]:

$$\sigma'_{ij} = \sigma_{ij} - p_f\beta_{ij} \tag{10}$$

where σ' is the effective stress, and the Biot tensor β is calculated from [*Carroll*, 1979]:

$$\beta_{ij} = \delta_{ij} - c_{ijkl}s^{i}_{klmm} \tag{11}$$

where c_{ijkl} is the stiffness of the damaged rock, s^{i}_{klmm} is the compliance of the intact rock, and δ is the Kronecker delta. The effective stress components vary according to the anisotropy in each layer, as a function of the Biot tensor. In the case of isotropy, the Biot coefficient tensor becomes the second-order identity tensor, and the only effect of the pore fluid pressure is on the normal stress components. In this formulation (equation 11), there is no explicit term for porosity. The effects of the pore space, whether true pores or damage-induced cracks, are included in the stiffness tensor of the damage rock (c_{ijkl}) calculated from EMT. For the crystalline granitic protoliths in this study, most of the porosity will be damage-induced cracks and accurately captured by the damaged stiffness tensor. However, for clastic sedimentary protoliths like sandstone, the original pore space could make a significant contribution and this would need to be calculated using an ellipsoidal (i.e., not penny-shaped) pore geometry.

[25] The elastic stiffnesses of the crack damage patterns listed in Table 2 have been calculated using the "dry" crack formulation of EMT. With the addition of poroelasticity and

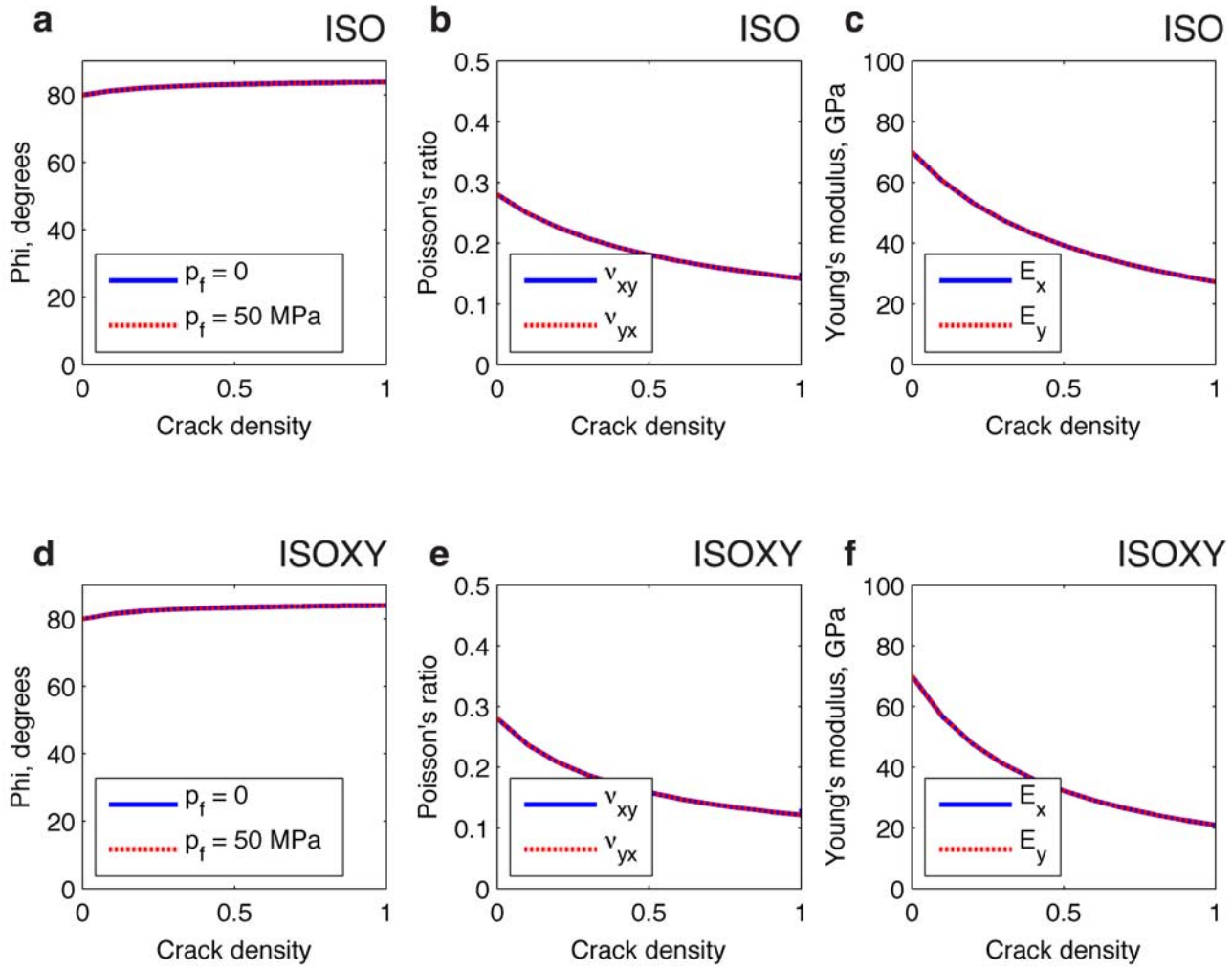

Figure 4. Stress rotations and elastic properties as a function of crack density for the ISO and ISOXY crack damage patterns. (a–c) Random crack damage (ISO pattern) results in rotation of σ_1 away from the fault plane by a few degrees, with Poisson's ratio and Young's modulus showing significant decreases with increasing crack density. (d–f) Cracks with poles in *xy* (ISOXY pattern) show the same trends, although with steeper changes in elastic properties with crack density.

effective stress to the elastic multilayer model to incorporate the effect of a pressurized pore fluid, this choice requires explanation. This "dry" crack formulation is the correct approximation for the static response of a saturated fault zone to long-term (e.g., interseismic) loads. The elastic response of saturated rocks is frequency dependent [see *Guéguen and Boutéca*, 2004, chap. 1 and 4]. For high-frequency (ultrasonic, MHz) measurements on laboratory scale samples the "wet" fluid-filled crack formulation of EMT accurately captures the elastic response [*Guéguen and Schubnel*, 2003]. Subjected to loads at these high frequencies, the fluid in the rock is stationary within the pores, corresponding to the "undrained" case of poroelasticity. However, for static loads (and very low frequencies), the fluid is able to move in the pores over the time scale of the loading, corresponding to the "drained" approximation of poroelasticity. In the anisotropic poroelastic multilayer model of a fault zone the "drained" approximation implies that the pore fluid pressure is constant across the whole damage zone and that the boundary conditions of constant fault-normal stress (σ_{yy}) and fault-parallel shear stress (τ_{xy}) are borne by the solid skeleton.

[26] While pressurized pore fluids have long been postulated for the gouge-filled fault cores [*Chester et al.*, 1993], the presence of fluids in the damage zone is less obvious. However, field studies of exhumed major fault zones record abundant structural evidence in the form of fluid-assisted deformation mechanisms [*Chester and Logan*, 1986], healed fluid-inclusion planes [*Faulkner et al.*, 2006], and abundant evidence for hydration reactions involving epidote and chlorite [*Cembrano et al.*, 2005] in these damage zones.

7. Effect of Crack Patterns on Stress State in Fault Damage Zones

[27] Changes in elastic properties have been calculated for the initially intact and isotropic Cerro Cristales granodiorite for each of the damage patterns listed in Table 2. For each pattern, the stiffness was calculated for 10 layers in the multilayer model with crack densities ranging from 0.1 to

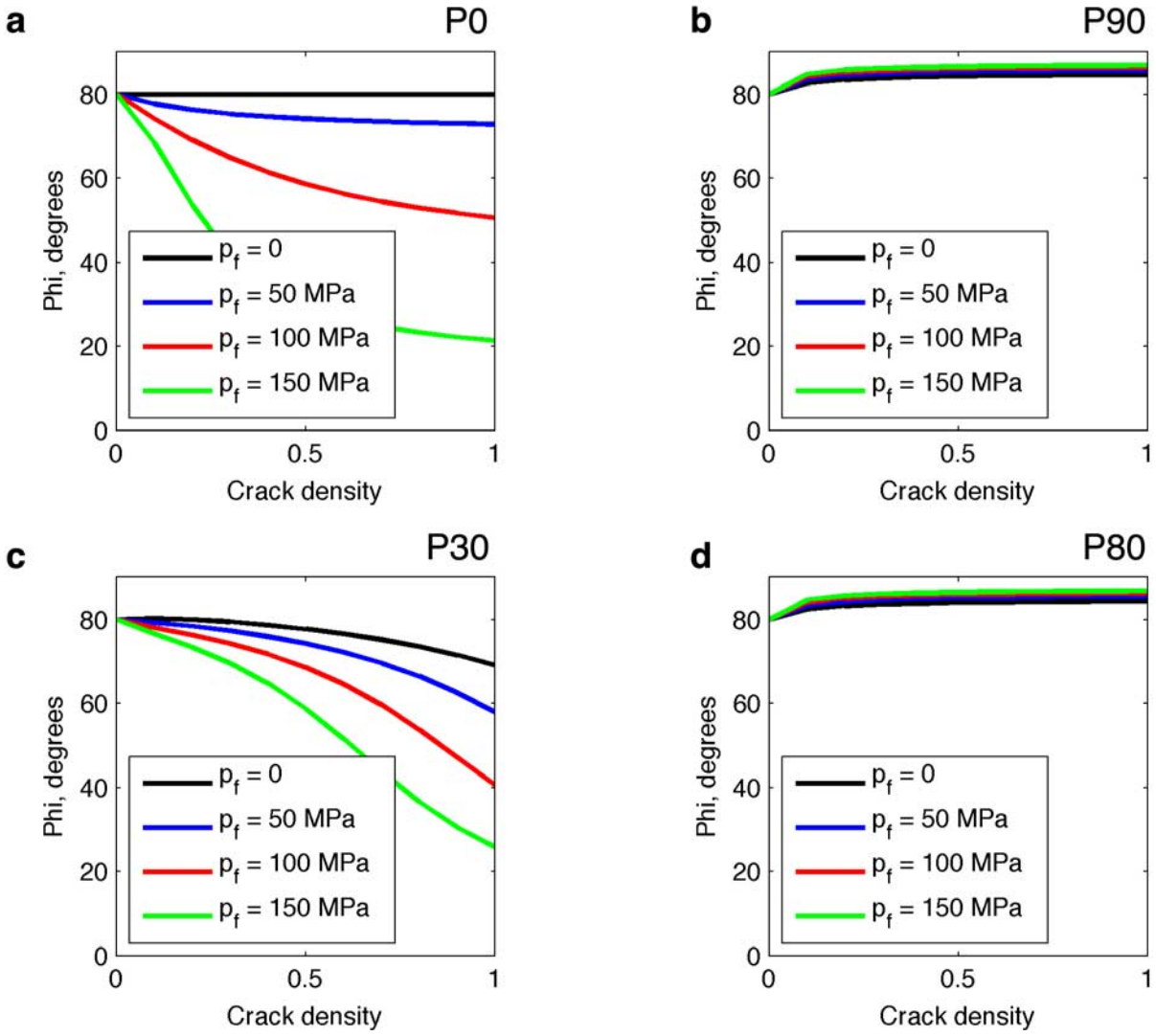

Figure 5. Rotation of σ_1' as a function of crack density for the parallel crack damage patterns. (a) P0 pattern (fault-parallel cracks), shows large rotations (low ϕ) for high pore fluid pressures and high crack densities. (b) P90 pattern (fault-normal cracks), shows small rotations away from the fault for all pore fluid pressures and crack densities. (c) Monoclinic low angle crack pattern P30 also shows rotations toward the fault for high crack density and high p_f. (d) P80 pattern, perhaps the most likely for a misoriented fault, shows small rotations away from the fault plane.

1.0. The fault zone multilayer was subjected to a remote stress field of σ_1 = 120 MPa at 80° to the fault and σ_3 = 60 MPa. The rotation of σ_1' (ϕ) was calculated for each layer for a range of pore fluid pressures, together with the values of E_x, E_y, ν_{xy} and ν_{yx} for the transversely isotropic and monoclinic layers. The granodiorite protolith and the remote stress field were selected to be representative of a strike-slip fault in continental crust, at a depth of 3–5 km, and severely misoriented with respect to the maximum compression direction.

7.1. Isotropic Crack Patterns

[28] Figure 4 shows the effect of the ISO and ISOXY patterns on ϕ. Neither pattern produces stress rotations toward the fault zone; in contrast, ϕ increases with crack density (Figures 4a and 4d). For these patterns (both isotropic in *xy*), elevated pore fluid pressure (p_f = 50 MPa) has no effect on ϕ. Calculated values of Poisson's ratio (Figures 4b and 4e) and Young's modulus (Figures 4c and 4f) both decrease with increasing crack density, in accord with observations from experiments conducted with nonzero confining pressure [*Brace et al.*, 1966; *Schubnel et al.*, 2003; *Katz and Reches*, 2004] and with in situ field measurements made by *Katz et al.* [2000]. The model results, based on the experimentally validated EMT and combined with a poroelastic multilayer model, cast further doubt on the relevance of the isotropic model used by *Faulkner et al.* [2006].

7.2. Anisotropic Crack Patterns

[29] The effect of anisotropic damage patterns on ϕ is shown in Figure 5 for a range of pore fluid pressures (0–150 MPa). Note that only the P0 and P30 damage patterns produce reductions in ϕ with increasing crack density

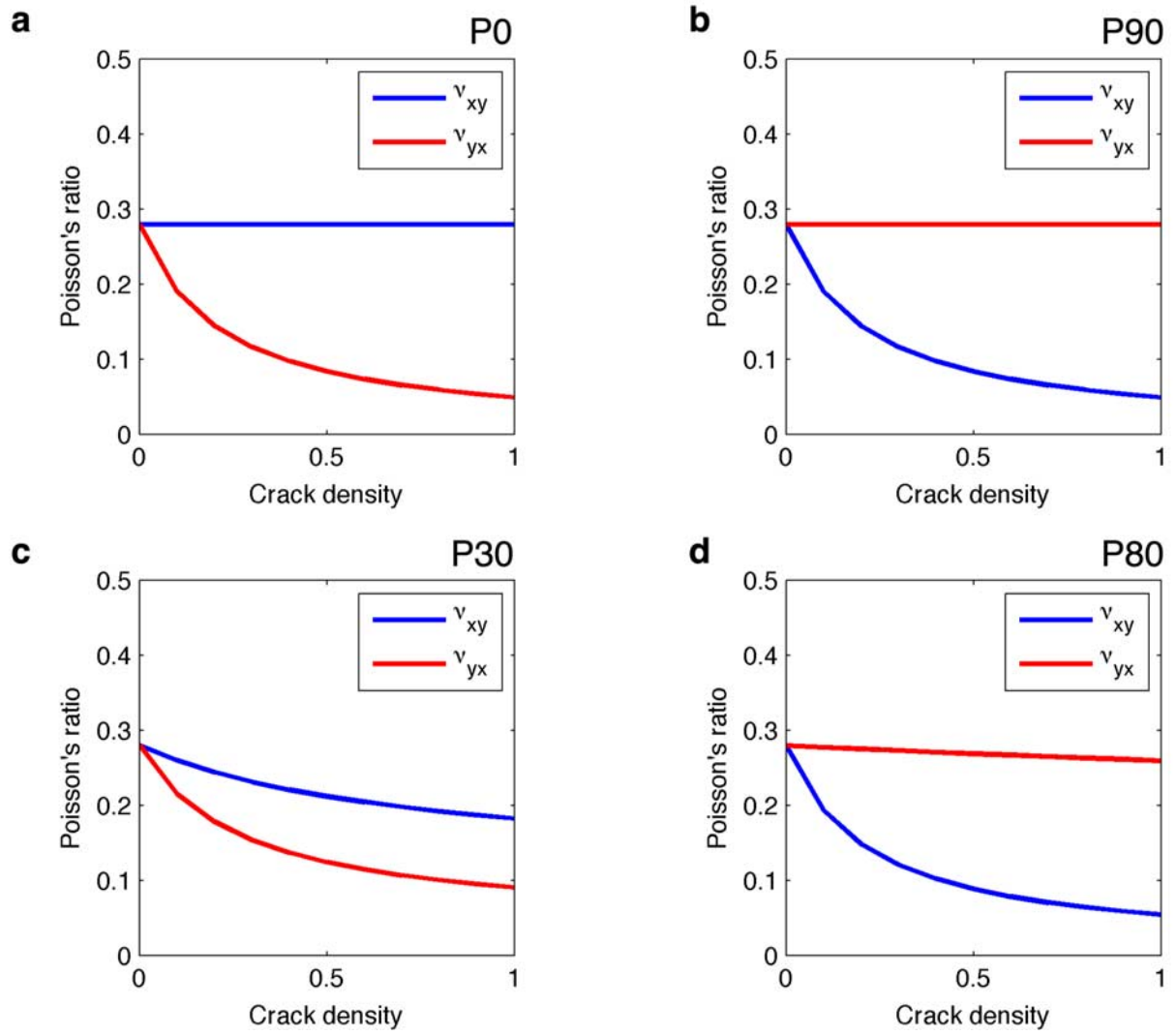

Figure 6. Poisson's ratio as a function of crack density for the parallel crack damage patterns. Initial value of 0.28 for the intact Cerro Cristales granodiorite. None of the damage patterns (P0, P90, P30, P80) generates increases in Poisson's ratio with increasing crack density.

(Figures 5a and 5c). Crack damage oriented at a high angle to the fault plane, exemplified by the P90 and P80 patterns (Figures 5b and 5d), results in rotation of σ_1' away from the fault plane, i.e., to more fault-normal orientations. For the P0 and P30 patterns, significant rotation of σ_1' toward the fault plane (i.e., $\phi < 40°$) is only possible with very high pore fluid pressures ($\gg$100 MPa). This is a direct result of the interaction between the broadly fault-parallel anisotropy in these patterns and the pore fluid pressure, described by the anisotropic effective stress law (equations (10) and (11)).

[30] The rotation of σ_1 away from the fault with the P90 and P80 patterns may appear counterintuitive, in that fault-normal cracks would suggest higher Poisson's ratios in the fault-parallel direction. As described in section 2, high values of Poisson's ratio in the isotropic case promote strong rotations of σ_1 toward the fault. However, for the anisotropic patterns the calculated values of Poisson's ratio in the fault-parallel direction (ν_{yx}) do *not* increase with crack density (Figures 6b and 6d) for these high angle patterns. Note that the rotation of σ_1' is controlled by the magnitude of σ_{xx} and p_f and not ε_{xx}. In a simplified uniaxial case, the value of ν_{yx} is $-\varepsilon_{xx}/\varepsilon_{yy}$ for a load applied in the y (fault-normal) direction. In the elastic multilayer model, the value of ε_{xx} is fixed, i.e., no slip between the layers, and the value of ε_{yy} depends on the Young's modulus in the loading direction (y in this case). E_y for the P90 and P80 damage patterns is shown in Figures 7b and 7d and decreases only slightly in the case of P80 and not at all for P90. The value of σ_{xx} that controls the rotation of σ_1 depends on several values of the stiffness tensor (equations (2) and (6)), and the orientation of σ_1' depends on p_f (equation (10)).

[31] For the P0 and P30 patterns, the values of ν_{yx} drop significantly with increasing crack density (Figures 6a and 6c), in tandem with small reductions in E_x (Figures 7a and 7c). This fault-parallel anisotropy combined with high pore fluid pressures can theoretically rotate σ_1' toward the fault (e.g., $\phi = \sim 20°$ for $p_f = 150$ MPa). Whether such high pore fluid pressures can be sustained in the damage zone of a large strike-slip fault is open to question. The values of p_f required to rotate σ_1' to within 30° ($\gg$100 MPa) represent

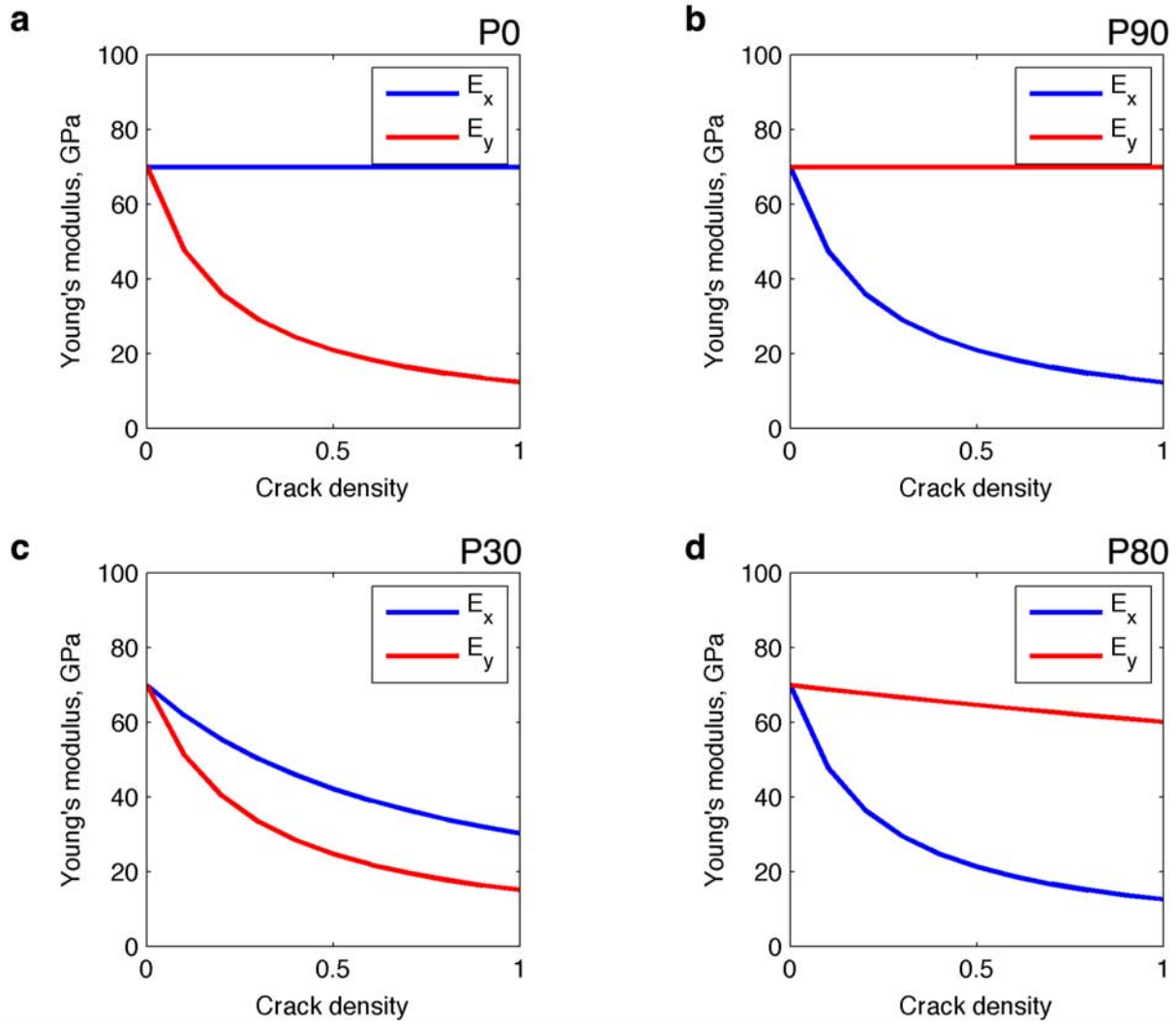

Figure 7. Young's modulus as a function of crack density for the parallel crack damage patterns. Initial value of 70 GPa for intact Cerro Cristales granodiorite. All of the damage patterns (P0, P90, P30, P80) generate decreases in Young's modulus with increasing crack density.

over twice the minimum compressive stress (σ_3 = 60 MPa) applied to the model. Figure 8 shows Mohr circles for the stress states of selected layers of the P30 and P80 damage patterns (crack densities of 0.3, 0.6, 0.9). For relatively low pore fluid pressures (Figures 8a and 8b; p_f = 50 MPa), the effects of anisotropic poroelasticity are clear: normal and shear stresses both change with p_f. For high angle damage patterns (P80) however, the increase in differential stress in these layers will encourage tensile failure (Figure 8b). At the very high pore fluid pressures (e.g., 150 MPa) required to rotate σ_1' to 30° of the fault, the rocks of the innermost damage zones in the P30 pattern could still be intact (Figure 8c), whereas a damage zone with high angle cracks will almost certainly have failed (Figure 8d).

8. Anisotropic Fault Core Zones

[32] The combination of fault-parallel anisotropy in the damage zones of natural faults described by the P0 and P30 patterns together with very high pore fluid pressures awaits field evidence. However, the more obvious site for this combination of anisotropy and pore fluid pressure is in the fault core zone where the bulk of the displacements are localized [*Chester et al.*, 1993]. In the absence of measured elasticity values for fault core rocks, the stress state of fault core zones can be modeled using measurements from lithologically similar rocks and then "add in" crack damage using the EMT formulation. Fault gouge and cataclasite are generally rich in clay minerals and carry a strong fault-parallel fabric [*Chester and Logan*, 1986; *Jefferies et al.*, 2006]. The permeability of fault core rocks is highly anisotropic with several orders of magnitude difference in the permeability measured across and along the gouge fabric [*Faulkner and Rutter*, 2001; *Wibberley and Shimamoto*, 2003]. This suggests a substantial connected porosity aligned parallel to the fault in the core zone, and this is supported by field data [*Katz et al.*, 2003, Figure 15]. The elastic properties of two fault gouges have been calculated for a simplified multilayer model (Figure 9), with a single core layer surrounded by an isotropic intact protolith (Cerro Cristales granodiorite). The measured intact stiffness values

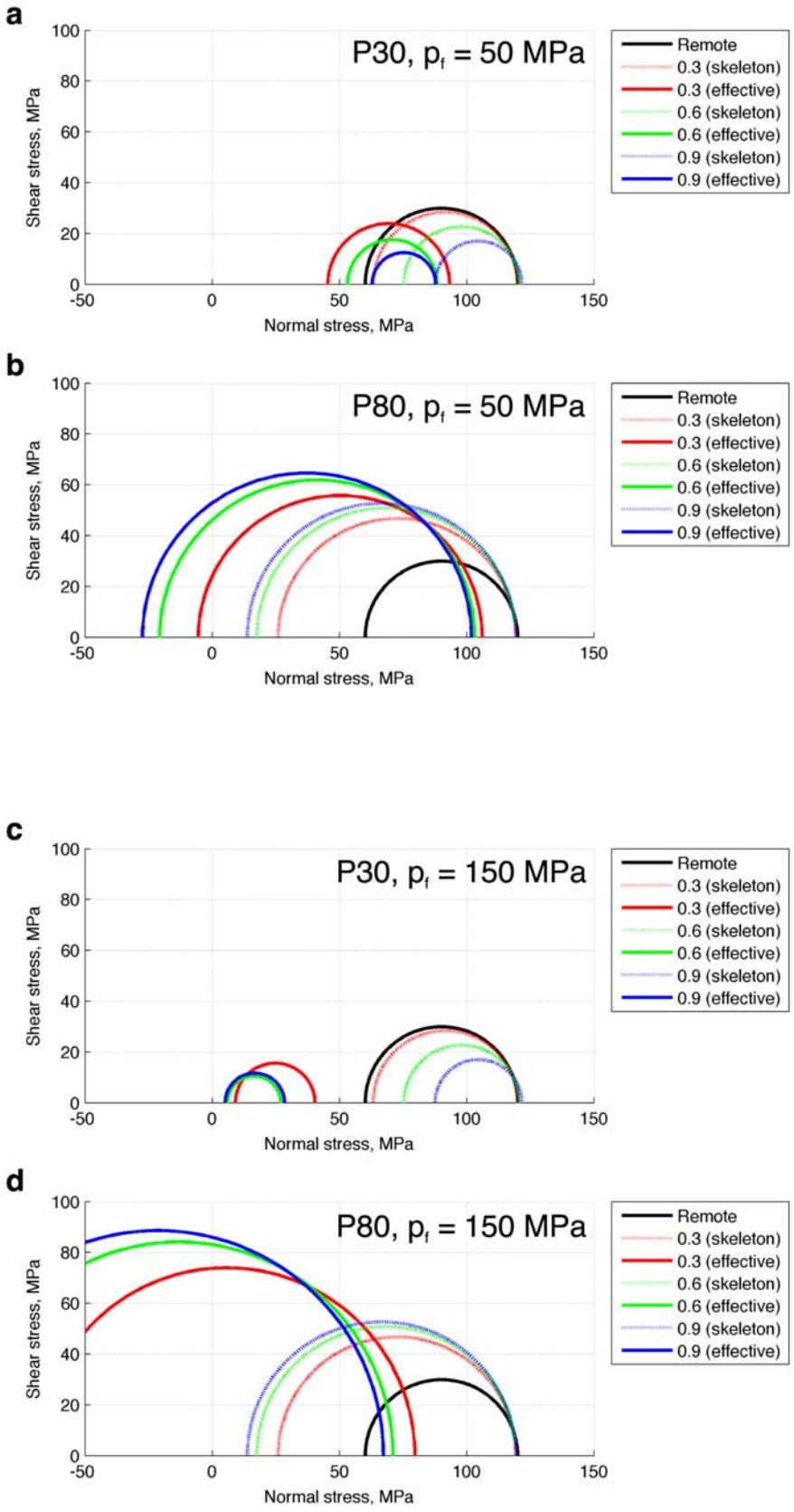

Figure 8. Stress states in selected damage zone layers for P30 and P80 crack damage patterns. The remote loading stress state is show by the black semicircle in each case (σ_1 = 120 MPa, σ_3 = 60 MPa, ϕ = 80). The solid skeleton and effective stresses for three damage zone layers corresponding to crack densities of 0.3, 0.6, and 0.9 are shown for the P30 and P80 damage patterns at two pore fluid pressures (50 MPa and 150 MPa). The effective stress in P80 pattern leads to tensile failure in both cases.

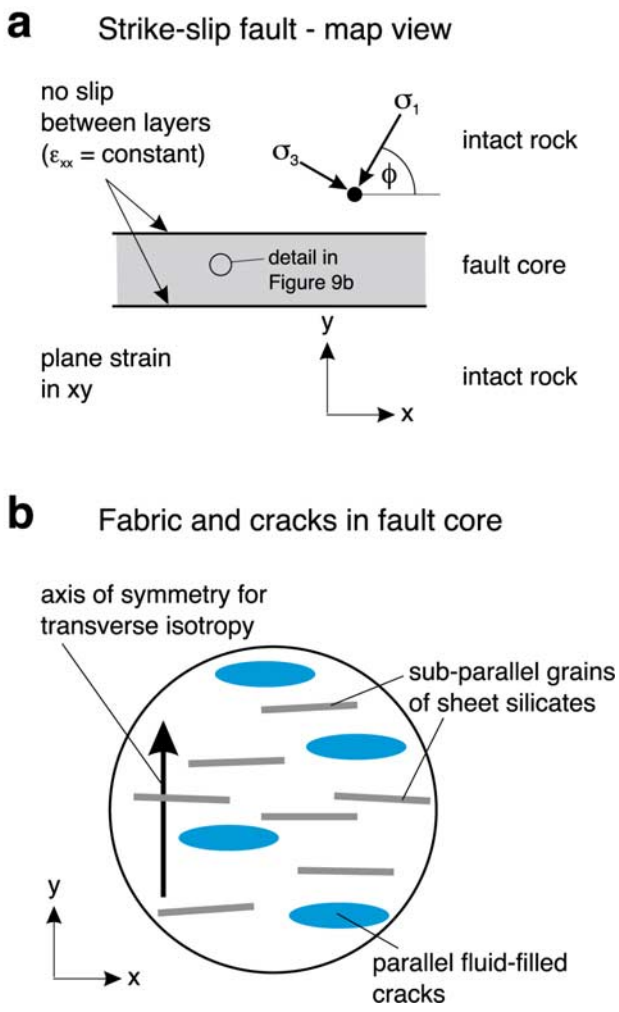

Figure 9. Configuration of the simplified multilayer model for the fault core zone. (a) Schematic view of a single fault core zone (gray layer) within an intact matrix. (b) Detail of the anisotropic fabric in the core zone rock, and the orientation of the transverse isotropy symmetry axis (parallel to y).

of selected analogs for core zone rocks (Table 3) were combined with a calculated component using a P0 damage pattern with a crack density of 1.0. The elastic stiffness values of shale ("Shale 1" taken from *Vavrycuk* [2005]) measured at 70 MPa confining pressure, and serpentinite (taken from *Song et al.* [2004]) measured at 80 MPa confining pressure, are used as proxies for the intact properties of two fault gouges, both relevant to the San Andreas Fault [*Chester et al.*, 1993; *Moore and Rymer*, 2007]. Note that although the gouge layers differ markedly in composition from the surrounding protolith, the mechanical basis of the elastic multilayer model is still valid for the static stress case. In natural examples, it is highly likely that slip events will nucleate at the contact between the gouge and the host rock, but in between these discrete seismic events the boundary is accurately described by a no-slip condition.

[33] Figure 10 shows the variation in ϕ with pore fluid pressure calculated using the anisotropic poroelastic model. The remote stress is the same as that applied to the damage zone models (σ_1 = 120 MPa at 80° to the fault and σ_3 = 60 MPa). The shale fault core is highly anisotropic, and ϕ falls to <60° even with zero pore fluid pressure (Figure 10a). With increasing crack density and pore fluid pressure, ϕ falls to <40° at ~100 MPa of pore fluid pressure (Figure 10a, red and blue curves). For the serpentinite core, the change is more dramatic, with ϕ dropping to <20° at ~130 MPa pore fluid pressure. These extreme rotations are again the result of the combination of the fault-parallel anisotropy with high pore fluid pressures (equations (10) and (11)). The stress states shown in Figures 11 and 12 confirm that even for p_f > 100 MPa, these fault core zone rocks will not fail in tension. Therefore, high pore fluid pressures can be sustained by the rocks in the core and simultaneously promote rotations of σ_1' to less than 40°.

9. Discussion

9.1. Model Parameters

[34] The models use a maximum scalar crack density of 1.0 which, although high, is still compatible with the NIA of EMT. This limit must be small enough to sustain the fundamental elastic assumption of the model, which inevitably breaks down at even higher crack densities as the rock mass loses integrity. On the basis of a comparison of the theoretical predictions with laboratory experiments, *Schubnel et al.* [2006] found an acceptable fit up to a scalar crack density of 0.5 but observed that at failure, the crack density approached 1. In separate experiments, *Katz and Reches* [2004] report scalar crack densities >0.4 in the localized zones around the failure plane. The models employ a constant crack radius of 0.01 m (1 cm). Qualitative observations of natural fault damage zones suggest a wide distribution of crack sizes. A power law distribution of lengths is often postulated for fracture populations, but field studies have yet to report systematic measurements of fracture lengths in relation to distance from the fault plane, from within fault damage or core zones. A further caveat is that the new model is based on EMT and the Non-Interaction Approximation, which in turn assumes a random spatial distribution of crack centers. In the absence of

Table 3. Elastic Constants of Intact Rocks Used in Fault Core Models

	ci1	*ci2*	*ci3*	*ci4*	*ci5*	*ci6*
			Shale[a]			
c1j	58.81	11.73	23.64	0.00	0.00	0.00
c2j	11.73	58.81	23.64	0.00	0.00	0.00
c3j	23.64	23.64	27.23	0.00	0.00	0.00
c4j	0.00	0.00	0.00	13.23	0.00	0.00
c5j	0.00	0.00	0.00	0.00	13.23	0.00
c6j	0.00	0.00	0.00	0.00	0.00	23.54
			Serpentinite[b]			
c1j	100.00	36.00	42.00	0.00	0.00	0.00
c2j	36.00	100.00	42.00	0.00	0.00	0.00
c3j	42.00	42.00	85.00	0.00	0.00	0.00
c4j	0.00	0.00	0.00	24.00	0.00	0.00
c5j	0.00	0.00	0.00	0.00	24.00	0.00
c6j	0.00	0.00	0.00	0.00	0.00	34.00

[a] "Shale 1" from *Vavrycuk* [2005]. Stiffness tensor c_{ij} (Voigt notation, units are GPa).
[b] *Song et al.* [2004]. Stiffness tensor c_{ij} (Voigt notation, units are GPa).

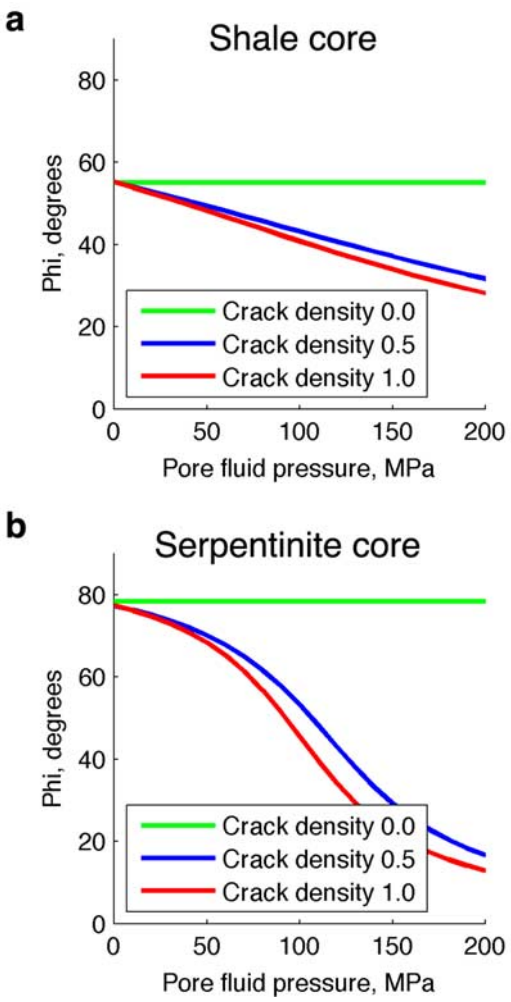

Figure 10. Stress rotations in fault core zones as a function of pore fluid pressure. For both the (a) shale core and (b) serpentinite core the effect of pore fluid pressure combined with the strong anisotropy (mineral fabric plus fault-parallel crack damage) results in large rotations of σ_1' toward the fault for nonzero crack densities.

detailed microstructural observations, this assumption appears to be reasonable, but further data are required from naturally faulted rocks to test this.

9.2. Extrapolating Experimental Data to Natural Cases

[35] The validity of extrapolating measurements from uniaxial unconfined rock deformation experiments to the truly triaxial confined conditions at depth likely along a major strike-slip fault has already been questioned, but the measurements of E, and especially ν, still stand as observations [*Heap and Faulkner*, 2008]. Given the predictions of the model for the ISO and ISOXY damage patterns (i.e., σ_1 rotating slightly away from the fault), the "mapping" of the experimental measurements from the transversely isotropic (axial) symmetry of the uniaxial deformation to an isotropic elastic stiffness tensor by *Faulkner et al.* [2006], without any assessment of the crack damage pattern in the sample, is highly questionable. It is instructive to compare the intact (Table 4, top) and damaged (Table 4, bottom) stiffness tensors before and after deformation of the Westerly granite "mapped" according to the method used by [*Faulkner et al.*, 2006]. The values of the damaged stiffness coefficients (Table 4, bottom) dramatically increase, in stark contrast to previous experimental measurements of elastic properties [e.g., *Brace et al.*, 1966; *Schubnel et al.*, 2003; *Katz and Reches*, 2004]. Scope exists to integrate truly triaxial experimental measurements of elastic stiffness with observations of crack damage patterns in the sample, before extrapolating to the scale of crustal fault zone.

9.3. Complexity in Natural Fault Zones

[36] Damage processes in the fault tip region during fault growth and the dynamic effects of slip pulses on the wall rocks of mature faults can produce asymmetry in crack damage patterns on either side of the fault core [*Vermilye and Scholz*, 1998; *Rice et al.*, 2005]. The models presented in this paper assume homogeneous patterns along layers parallel to the master fault. *Wilson et al.* [2003] have also shown that even on one side of a mature fault, the damage pattern is not uniform, with fault-parallel crack patterns at some distance from the fault giving way to fault-normal crack patterns in the innermost damage zone. These observations suggest that in natural fault zones stress trajectories are unlikely to be monotonically increasing or decreasing functions of distance from the core, but more likely to be irregular and "wavy." Field studies of fault damage zones

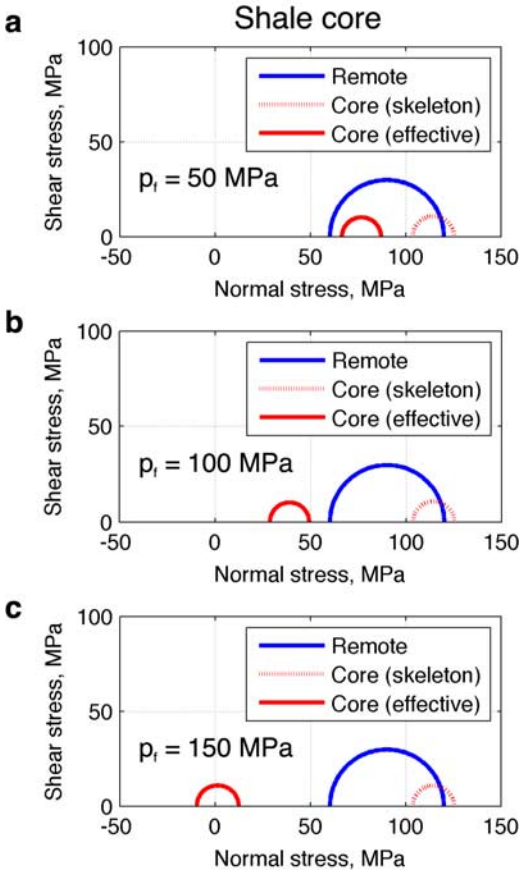

Figure 11. Stress states in the shale fault core at three different pore fluid pressures (50, 100, and 150 MPa). Tensile failure is only predicted at $p_f \gg 100$ MPa within the anisotropic shale core.

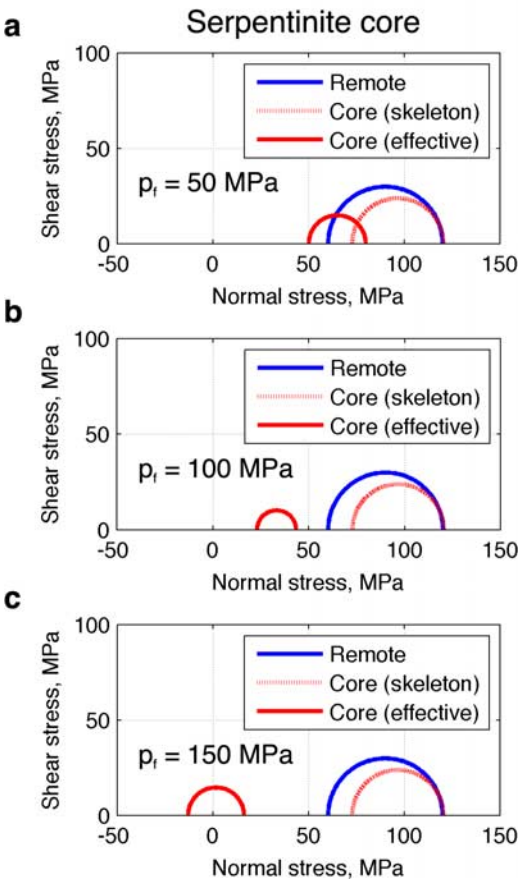

Figure 12. Stress states in the serpentinite fault core at three different pore fluid pressures (50, 100, and 150 MPa). Tensile failure is only predicted at $p_f \gg 100$ MPa within the anisotropic serpentinite core.

have extensively documented the exponential increase in crack density toward the fault core [*Anders and Wiltschko*, 1994; *Vermilye and Scholz*, 1998; *Wilson et al.*, 2003], but these studies do not consider along strike variations in either damage intensity or pattern. The lateral continuity of the patterns modeled in this paper needs to be tested with detailed field measurements.

9.4. Application to the San Andreas Fault, California

[37] Inhomogeneous stress has been documented around the San Andreas Fault (SAF). *Jones* [1988] used focal mechanism data to determine the orientation of stress around the SAF in southern California and found that while the maximum horizontal stress (σ_H) varies along the strike of the SAF, it is not anywhere significantly rotated from the regional direction. *Provost and Houston* [2001] also used focal mechanisms, this time in the central California creeping section of the SAF, and found the highest values of ϕ closest to the fault, with the lowest values actually on the fault trace [*Provost and Houston*, 2001, Figures 7 and 8]. This is consistent with damage zone models using the P80 crack pattern. Sustained misorientation of the remote stress at a high angle (e.g., 80° to the fault) will lead to cracks in a similar high-angle orientation; the local effect of these cracks is to rotate σ_1 further away from the fault. The detailed fieldwork of *Chester et al.* [1993] around the San Gabriel and Punchbowl fault strands of the SAF documents the extreme localization of slip in this fault system. The record of veining, mineralization, and diffusive mass transfer processes in the narrow fault core zone also attests to elevated pore fluid pressures [*Chester et al.*, 1993]. Shear wave velocity data from local earthquakes indicate that fault-parallel fast polarizations are confined to stations located on the active fault traces [*Boness and Zoback*, 2006]. This suggests that the causative fault-parallel anisotropy of physical properties is also highly localized. Earlier work reported that this shear wave polarization is not related to fracture directions in the SAFOD Pilot Hole, located well within the SAF damage zone [*Boness and Zoback*, 2004]. These observations and interpretations from this highly studied crustal-scale fault zone are consistent with the presented models which show that large stress rotations are probable only in the anisotropic fault core rocks.

10. Summary

[38] The models presented in this paper have explored the influence of different crack damage patterns on the elastic properties of rocks in fault zones, with reference to stress rotations. This is a summary of the key findings from the anisotropic poroelastic fault zone model:

[39] 1. Rotations of σ_1 toward the fault in the damage zone only occurs for an unlikely combination of low angle cracks, highly misoriented σ_1, and extremely high pore fluid pressure.

[40] 2. Small rotations of σ_1 away from the fault in the damage zone occur for high angle cracks and high angle σ_1, consistent with field observations of crack damage patterns and in situ measurements of stress from focal mechanisms.

[41] 3. Significant rotations of σ_1 toward the fault are restricted to the fault core with highly anisotropic fault rocks containing strong mineral fabrics and fault-parallel crack damage, under conditions of elevated pore fluid pressure. The angle between σ_1 and the fault can reduce to <30° for shale and serpentinite dominated cores.

[42] 4. High pore fluid pressures in the anisotropic core will not result in tensile failure, and subsequent drainage of

Table 4. Elastic Constants of Intact and Deformed Westerly Granite

	ci1	*ci2*	*ci3*	*ci4*	*ci5*	*ci6*
			Intact[a]			
c1j	84.97	31.43	31.43	0.00	0.00	0.00
c2j	31.43	84.97	31.43	0.00	0.00	0.00
c3j	31.43	31.43	84.97	0.00	0.00	0.00
c4j	0.00	0.00	0.00	26.77	0.00	0.00
c5j	0.00	0.00	0.00	0.00	26.77	0.00
c6j	0.00	0.00	0.00	0.00	0.00	26.77
			Damaged[b]			
c1j	348.53	309.07	309.07	0.00	0.00	0.00
c2j	309.07	348.53	309.07	0.00	0.00	0.00
c3j	309.07	309.07	348.53	0.00	0.00	0.00
c4j	0.00	0.00	0.00	19.73	0.00	0.00
c5j	0.00	0.00	0.00	0.00	19.73	0.00
c6j	0.00	0.00	0.00	0.00	0.00	19.73

[a] *Heap and Faulkner* [2008]. Intact stiffness tensor c_{ij}. Voigt notation, units are GPa. E = 68 GPa, ν = 0.27.
[b] Voigt notation, units are GPa. E = 58 GPa, ν = 0.47.

the pore fluid, due to the anisotropic poroelastic coupling of shear and normal stresses.

[43] The weight of evidence from stress measurements based on focal mechanisms and field studies of damage patterns and fault rocks are consistent with the model results presented in this paper: significant stress rotations are restricted to the highly anisotropic fault rocks in the core zone under elevated pore fluid pressure. The weakness of unfavorably oriented faults is localized in the core zone and not due to stress rotations in the damage zone.

[44] **Acknowledgments.** This paper is dedicated to the memory of Martin Casey (Leeds), a great intellect and a great bloke. The author would like to thank Tom Mitchell (Hiroshima), Dan Faulkner (Liverpool), Dave Dewhurst (CSIRO), and Jon Kirby (TIGeR) for comments on early drafts of this manuscript; Joel Sarout (ENS) for preprints of unpublished work; reviewers Oded Katz and Alex Schubnel for detailed, constructive reviews that greatly improved the manuscript; and The Institute for Geoscience Research (TIGeR) at Curtin for funding a Fellowship. This is TIGeR publication 129.

References

Abers, G. A. (1991), Possible seismogenic shallow-dipping normal faults in the Woodlark-Dentrecasteaux extensional province, Papua-New-Guinea, *Geology*, *19*(12), 1205–1208, doi:10.1130/0091-7613(1991)019<1205:PSSDNF>2.3.CO;2.

Anders, M. H., and D. V. Wiltschko (1994), Microfracturing, paleostress and the growth of faults, *J. Struct. Geol.*, *16*(6), 795–815, doi:10.1016/0191-8141(94)90146-5.

Boness, N. L., and M. D. Zoback (2004), Stress-induced seismic velocity anisotropy and physical properties in the SAFOD Pilot Hole in Parkfield, CA, *Geophys. Res. Lett.*, *31*, L15S17, doi:10.1029/2003GL019020.

Boness, N. L., and M. D. Zoback (2006), Mapping stress and structurally controlled crustal shear velocity anisotropy in California, *Geology*, *34*(10), 825–828, doi:10.1130/G22309.1.

Brace, W. F., B. W. Paulding Jr., and C. Scholz (1966), Dilatancy in the fracture of crystalline rocks, *J. Geophys. Res.*, *71*(8), 3939–3953.

Byerlee, J. (1978), Friction of rocks, *Pure Appl. Geophys.*, *116*, 615–626.

Caine, J. S., J. P. Evans, and C. B. Forster (1996), Fault zone architecture and permeability structure, *Geology*, *24*(11), 1025–1028, doi:10.1130/0091-7613(1996)024<1025:FZAAPS>2.3.CO;2.

Carroll, M. M. (1979), An effective stress law for anisotropic elastic deformation, *J. Geophys. Res.*, *84*, 7510–7512.

Casey, M. (1980), Mechanics of shear zones in isotropic dilatant materials, *J. Struct. Geol.*, *2*(1–2), 143–147, doi:10.1016/0191-8141(80)90044-9.

Cembrano, J., G. Gonzalez, G. Arancibia, I. Ahumada, V. Olivares, and V. Herrera (2005), Fault zone development and strain partitioning in an extensional strike-slip duplex: A case study from the Mesozoic Atacama fault system, Northern Chile, *Tectonophysics*, *400*(1–4), 105–125, doi:10.1016/j.tecto.2005.02.012.

Chen, Q., and A. Nur (1992), Pore fluid pressure effects in anisotropic rocks: Mechanisms of induced seismicity and weak faults, *Pure Appl. Geophys.*, *139*(3), 463–479.

Chéry, J., M. D. Zoback, and R. Hassani (2001), An integrated mechanical model of the San Andreas fault in central and northern California, *J. Geophys. Res.*, *106*, 22,051–22,066, doi:10.1029/2001JB000382.

Chester, F. M., and J. M. Logan (1986), Implications for mechanical-properties of brittle faults from observations of the Punchbowl fault zone, California, *Pure Appl. Geophys.*, *124*(1–2), 79–106, doi:10.1007/BF00875720.

Chester, F. M., J. P. Evans, and R. L. Biegel (1993), Internal structure and weakening mechanisms of the San Andreas fault, *J. Geophys. Res.*, *98*, 771–786, doi:10.1029/92JB01866.

Chester, F. M., J. S. Chester, D. L. Kirschner, S. E. Schulz, and J. P. Evans (2004), Structure of large-displacement, strike-slip fault zones in the brittle continental crust, in *Rheology and Deformation in the Lithosphere at Continental Margins*, edited by G. D. Karner et al., pp. 223–260, Columbia Univ. Press, New York.

Collettini, C., and M. R. Barchi (2002), A low-angle normal fault in the Umbria region (Central Italy): A mechanical model for the related microseismicity, *Tectonophysics*, *359*(1–2), 97–115, doi:10.1016/S0040-1951(02)00441-9.

Faulkner, D. R., and E. H. Rutter (2001), Can the maintenance of overpressured fluids in large strike-slip fault zones explain their apparent weakness?, *Geology*, *29*(6), 503–506, doi:10.1130/0091-7613(2001)029<0503:CTMOOF>2.0.CO;2.

Faulkner, D. R., T. M. Mitchell, D. Healy, and M. J. Heap (2006), Slip on 'weak' faults by the rotation of regional stress in the fracture damage zone, *Nature*, *444*(7121), 922–925, doi:10.1038/nature05353.

Flinn, D. (1977), Transcurrent faults and associated cataclasis in Shetland, *J. Geol. Soc.*, *133*(3), 231–247, doi:10.1144/gsjgs.133.3.0231.

González, G. (1999), Mecanismo y profundidad de emplazamiento del Plutón de Cerro Cristales, Cordillera de la Costa, Antofagasta, Chile, *Rev. Geol. Chile*, *26*, 43–66.

Grechka, V., and M. Kachanov (2006), Effective elasticity of fractured rocks: A snapshot of the work in progress, *Geophysics*, *71*(6), W45–W58, doi:10.1190/1.2360212.

Guéguen, Y., and M. Boutéca (2004), *Mechanics of Fluid Saturated Rocks*, Elsevier, New York.

Guéguen, Y., and A. Schubnel (2003), Elastic wave velocities and permeability of cracked rocks, *Tectonophysics*, *370*(1–4), 163–176, doi:10.1016/S0040-1951(03)00184-7.

Hardebeck, J. L., and E. Hauksson (1999), Role of fluids in faulting inferred from stress field signatures, *Science*, *285*(5425), 236–239, doi:10.1126/science.285.5425.236.

Healy, D., R. R. Jones, and R. E. Holdsworth (2006a), New insights into the development of brittle shear fractures from a 3-D numerical model of microcrack interaction, *Earth Planet. Sci. Lett.*, *249*(1–2), 14–28, doi:10.1016/j.epsl.2006.06.041.

Healy, D., R. R. Jones, and R. E. Holdsworth (2006b), Three-dimensional brittle shear fracturing by tensile crack interaction, *Nature*, *439*(7072), 64–67, doi:10.1038/nature04346.

Heap, M. J., and D. R. Faulkner (2008), Quantifying the evolution of static elastic properties as crystalline rock approaches failure, *Int. J. Rock Mech. Min. Sci.*, *45*(4), 564–573, doi:10.1016/j.ijrmms.2007.07.018.

Hirose, T., and M. Bystricky (2007), Extreme dynamic weakening of faults during dehydration by coseismic shear heating, *Geophys. Res. Lett.*, *34*, L14311, doi:10.1029/2007GL030049.

Jaeger, J. C., N. G. W. Cook, and R. W. Zimmerman (2007), *Fundamentals of Rock Mechanics*, 488 pp., Blackwell, Malden, Mass.

Jefferies, S. P., R. E. Holdsworth, C. A. J. Wibberley, T. Shimamoto, C. J. Spiers, A. R. Niemeijer, and G. E. Lloyd (2006), The nature and importance of phyllonite development in crustal-scale fault cores: An example from the Median Tectonic Line, Japan, *J. Struct. Geol.*, *28*(2), 220–235, doi:10.1016/j.jsg.2005.10.008.

Jones, L. M. (1988), Focal mechanisms and the state of stress on the San Andreas fault in southern California, *J. Geophys. Res.*, *93*, 8869–8891, doi:10.1029/JB093iB08p08869.

Kachanov, M. (1993), On the effective moduli of solids with cavities and cracks, *Int. J. Fract.*, *59*(1), R17–R21.

Katz, O., and Z. Reches (2004), Microfracturing, damage, and failure of brittle granites, *J. Geophys. Res.*, *109*, B01206, doi:10.1029/2002JB001961.

Katz, O., Z. Reches, and J. C. Roegiers (2000), Evaluation of mechanical rock properties using a Schmidt Hammer, *Int. J. Rock Mech. Min. Sci.*, *37*(4), 723–728, doi:10.1016/S1365-1609(00)00004-6.

Katz, O., Z. Reches, and G. Baer (2003), Faults and their associated host rock deformation: Part I. Structure of small faults in a quartz-syenite body, southern Israel, *J. Struct. Geol.*, *25*(10), 1675–1689, doi:10.1016/S0191-8141(03)00011-7.

Lockner, D. A., J. D. Byerlee, V. Kuksenko, A. Ponomarev, and A. Sidorin (1991), Quasi-static fault growth and shear fracture energy in granite, *Nature*, *350*(6313), 39–42, doi:10.1038/350039a0.

McGarr, A. (1988), On the state of lithospheric stress in absence of applied tectonic forces, *J. Geophys. Res.*, *93*, 13,609–13,617, doi:10.1029/JB093iB11p13609.

Moore, D. E., and M. J. Rymer (2007), Talc-bearing serpentinite and the creeping section of the San Andreas fault, *Nature*, *448*(7155), 795–797, doi:10.1038/nature06064.

O'Connell, R. J., and B. Budiansky (1974), Seismic velocities in dry and saturated cracked solids, *J. Geophys. Res.*, *79*, 5412–5426, doi:10.1029/JB079i035p05412.

Provost, A. S., and H. Houston (2001), Orientation of the stress field surrounding the creeping section of the San Andreas Fault: Evidence for a narrow mechanically weak fault zone, *J. Geophys. Res.*, *106*, 11,373–11,386, doi:10.1029/2001JB900007.

Rabbel, W., et al. (2004), Superdeep vertical seismic profiling at the KTB deep drill hole (Germany): Seismic close-up view of a major thrust zone down to 8.5 km depth, *J. Geophys. Res.*, *109*, B09309, doi:10.1029/2004JB002975.

Reches, Z., and D. A. Lockner (1994), Nucleation and growth of faults in brittle rocks, *J. Geophys. Res.*, *99*, 18,159–18,173, doi:10.1029/94JB00115.

Rice, J. R. (1992), Fault stress states, pore pressure distributions, and the weakness of the San Andreas Fault, in *Fault Mechanics and Transport Properties in Rocks*, edited by B. Evans and T.-F. Wong, pp. 475–503, Academic, London.

Rice, J. R., C. G. Sammis, and R. Parsons (2005), Off-Fault Secondary Failure Induced by a Dynamic Slip Pulse, *Bull. Seismol. Soc. Am.*, *95*(1), 109–134, doi:10.1785/0120030166.

Sayers, C. M., and M. Kachanov (1995), Microcrack-induced elastic-wave anisotropy of brittle rocks, *J. Geophys. Res.*, *100*, 4149–4156, doi:10.1029/94JB03134.

Schubnel, A., O. Nishizawa, K. Masuda, X. J. Lei, Z. Xue, and Y. Gueguen (2003), Velocity measurements and crack density determination during wet triaxial experiments on Oshima and Toki granites, *Pure Appl. Geophys.*, *160*(5), 869–887, doi:10.1007/PL00012570.

Schubnel, A., P. M. Benson, B. D. Thompson, J. F. Hazzard, and R. P. Young (2006), Quantifying damage, saturation and anisotropy in cracked rocks by inverting elastic wave velocities, *Pure Appl. Geophys.*, *163*(5–6), 947–973, doi:10.1007/s00024-006-0061-y.

Song, I., M. Suh, Y. K. Woo, and T. Hao (2004), Determination of the elastic modulus set of foliated rocks from ultrasonic velocity measurements, *Eng. Geol. Amsterdam*, *72*(3–4), 293–308, doi:10.1016/j.enggeo.2003.10.003.

Vavrycuk, V. (2005), Focal mechanisms in anisotropic media, *Geophys. J. Int.*, *161*(2), 334–346, doi:10.1111/j.1365-246X.2005.02585.x.

Vermilye, J. M., and C. H. Scholz (1998), The process zone: A microstructural view of fault growth, *J. Geophys. Res.*, *103*, 12,223–12,237, doi:10.1029/98JB00957.

Wibberley, C. A. J., and T. Shimamoto (2003), Internal structure and permeability of major strike-slip fault zones: The Median Tectonic Line in Mie prefecture, southwest Japan, *J. Struct. Geol.*, *25*(1), 59–78, doi:10.1016/S0191-8141(02)00014-7.

Wibberley, C. A. J., and T. Shimamoto (2005), Earthquake slip weakening and asperities explained by thermal pressurization, *Nature*, *436*(7051), 689–692, doi:10.1038/nature03901.

Wilson, J. E., J. S. Chester, and F. M. Chester (2003), Microfracture analysis of fault growth and wear processes, Punchbowl Fault, San Andreas System, California, *J. Struct. Geol.*, *25*(11), 1855–1873, doi:10.1016/S0191-8141(03)00036-1.

Zoback, M. D., M. Zoback, V. Mount, J. Suppe, J. P. Eaton, J. H. Healy, D. Oppenheimer, P. Reasenberg, L. Jones, and C. B. Raleigh (1987), New evidence on the state of stress of the San Andreas Fault System, *Science*, *238*(4830), 1105–1111.

D. Healy, The Institute for Geoscience Research, Department of Applied Geology, Curtin University of Technology, GPO Box U1987, Perth, WA 6845, Australia. (d.healy@curtin.edu.au)